Curvature of the pseudocritical line in the QCD phase diagram from mesonic lattice correlation functions

Antonio Smecca,[1,*] Gert Aarts,[1] Chris Allton,[1] Ryan Bignell,[2] Benjamin Jäger,[3] Seung-il Nam,[4] Seyong Kim,[5] Jon-Ivar Skullerud,[6,2] and Liang-Kai Wu[7]

[1]*Centre for Quantum Fields and Gravity, Department of Physics, Swansea University, Swansea, SA2 8PP, United Kingdom*
[2]*School of Mathematics, Trinity College Dublin, Dublin, Ireland*
[3]*Quantum Field Theory Center and Danish IAS, Department of Mathematics and Computer Science University of Southern Denmark, 5230, Odense M, Denmark*
[4]*Department of Physics, Pukyong National University (PKNU), Busan 48513, Korea*
[5]*Department of Physics, Sejong University, Seoul 143-747, Korea*
[6]*Department of Physics and Hamilton Institute, National University of Ireland Maynooth, County Kildare, Ireland*
[7]*School of Physics and Electronic Engineering, Jiangsu University, Zhenjiang 212013, China and Key Laboratory of Quark and Lepton Physics (MOE), Central China Normal University, Wuhan 430079, China*

(Received 16 February 2025; accepted 24 November 2025; published 15 December 2025)

In the QCD phase diagram, the dependence of the pseudocritical temperature, $T_{\rm pc}$, on the baryon chemical potential, μ_B, is of fundamental interest. The variation of $T_{\rm pc}$ with μ_B is normally captured by κ, the coefficient of the leading (quadratic) term of the polynomial expansion of $T_{\rm pc}$ with μ_B. In this work, we present the first calculation of κ using hadronic quantities. Simulating $N_f = 2+1$ flavors of Wilson fermions on Fastsum ensembles, we calculate the $\mathcal{O}(\mu_B^2)$ correction to mesonic correlation functions. By demanding degeneracy in the vector and axial-vector channels we obtain $T_{\rm pc}(\mu_B)$ and hence κ. While lacking a continuum extrapolation and being away from the physical point, our results are consistent with previous works using thermodynamic observables (renormalized chiral condensate, strange quark number susceptibility) from lattice QCD simulations with staggered fermions.

DOI: 10.1103/wjm8-4smh

I. INTRODUCTION

A complete understanding of the phase diagram of quantum chromodynamics (QCD) in the temperature, T, and baryonic chemical potential, μ_B, plane remains an open question in particle physics. The current understanding is that at $\mu_B = 0$ a smooth crossover at a pseudocritical temperature $T_{\rm pc}$ separates the low-T phase, characterized by broken chiral symmetry, from the high-T phase, in which chiral symmetry is restored [1]. This is supported by numerous lattice QCD studies [2–5], the only nonperturbative *ab initio* method for calculations in QCD.

Of particular interest is the determination of the pseudocritical curve, $T_{\rm pc}(\mu_B)$, in the $T-\mu_B$ plane. Lattice studies have shown that $T_{\rm pc}$ decreases with μ_B [4,6,7], and it has been argued that the crossover turns into a first-order phase transition for sufficiently large values of μ_B [8]. At the critical end point, separating the crossover and the first-order transition, the transition is expected to be second order. Unfortunately, direct lattice simulations are restricted to $\mu_B = 0$ due to the sign problem [9,10]. This problem can be circumvented by simulations at imaginary μ_B [11–26] or by a Taylor expansion of physical observables in μ_B/T around $\mu_B = 0$ [6,27–29]. Both methods are most accurate near $\mu_B = 0$. The pseudocritical curve can then be expressed as

$$\frac{T_{\rm pc}(\mu_B)}{T_{\rm pc}(\mu_B=0)} = 1 - \kappa\left(\frac{\mu_B}{T_{\rm pc}(\mu_B=0)}\right)^2 + \mathcal{O}(\mu_B^4), \qquad (1)$$

where κ is the curvature; see the review [30].

Thus far, observables used to determine $T_{\rm pc}(\mu_B)$ and calculate κ are directly obtainable from the QCD partition function, namely the renormalized chiral condensate and the strange quark number susceptibility; see e.g.

*Contact author: antonio.smecca@swansea.ac.uk

Refs. [5,31–39] for studies with (partially) chirally symmetric actions at or close to the physical point and extrapolated to the continuum limit. In this work we introduce a new lattice approach based on hadronic physics. We first expand mesonic correlation functions as a Taylor series in μ_B and note that in the presence of chiral symmetry a degeneracy is expected for correlation functions in the light vector and axial-vector meson channels. By mapping out the temperature where this degeneracy occurs as a function of μ_B, we determine the pseudocritical curve, $T_{\rm pc}(\mu_B)$, and hence κ.

The paper is organised as follows: in Sec. II we introduce the lattice ensembles and the quantities used in the analysis, in Sec. III we present the numerical results, in Sec. IV we discuss the systematic effects that could affect our calculation, and in Sec. V we summarize our conclusions. Preliminary results for mesonic correlation functions at nonzero μ_B can be found in Ref. [40].

II. METHODOLOGY

In our investigation we used two sets of Fastsum Collaboration lattice ensembles with $\mu_B = 0$, labeled "Generation 2" and "Generation 2L." These are generated using $N_f = 2 + 1$ dynamical fermions, setting the up and down quarks to be degenerate and with an approximately physical strange quark. We employ anisotropic lattices with $a_\tau/a_s \ll 1$ to increase the number of data points in the temporal direction. The fermions and gauge fields are simulated using the $\mathcal{O}(a)$-improved Wilson fermion action with stout-smeared links and a Symanzik-improved gauge action respectively. We use a fixed-scale approach where the temperature $T = 1/(a_\tau N_\tau)$ changes by varying N_τ with a_τ kept fixed. While the lattice spacings of the two ensembles are nearly the same, the Generation 2L pion mass is much lighter than in Generation 2, albeit still heavier than in nature. Tables I and II summarize the important features of the Generation 2 and Generation 2L ensembles. Further details can be found in Refs. [41,42] and [43–45] respectively.

We compute meson correlation functions projected to zero momentum,

$$G(\tau) = \langle J_H(\tau) J_H^\dagger(0)\rangle \equiv \langle g(\tau)\rangle_B, \tag{2}$$

where $J_H = \bar\psi \Gamma_H \psi$ is a meson operator in the isotriplet channel H, with Γ_H the appropriate combination of γ matrices to match the quantum numbers of the desired state, $g(\tau) \equiv \langle J_H(\tau) J_H^\dagger(0)\rangle_F$ is the correlator averaged over fermionic degrees of freedom only, and $\langle . \rangle_B$ represents an average over the bosonic (gauge) degrees of freedom.

Following Refs. [40,48,49], we expand the correlator to second order in μ_q/T,

TABLE I. Generation 2 and Generation 2L ensembles. The pseudocritical temperature $T_{\rm pc}(\mu_B = 0)$ is determined via the inflection point of the renormalized chiral condensate $\langle\bar\psi\psi\rangle_R$. As expected, the value depends on the pion mass M_π. The temporal (spatial) lattice spacings are $a_{\tau(s)}$, while the number of spatial points is N_s. For each generation the mass of the Ω baryon was used to determine a_τ [46,47]. Here, the Generation 2 value has been updated compared to our previous work [41], using the analysis presented in Ref. [46] by the HadSpec Collaboration. Further details can be found in Refs. [41,42] (Generation 2) and [43–45] (Generation 2L).

	Generation 2	Generation 2L
M_π [MeV]	391(3)	239(1)
$T_{\rm pc}$ [MeV]	182(2)	167(3)
a_τ [fm]	0.03482(26)	0.03246(7)
a_s [fm]	0.11992(92)	0.11208(31)
N_s	24	32

$$G(\tau;\mu_q) = G(\tau;\mu_q)|_{\mu_q=0} + \frac{\mu_q}{T} T \left.\frac{\partial G(\tau;\mu_q)}{\partial \mu_q}\right|_{\mu_q=0} + \frac{1}{2}\frac{\mu_q^2}{T^2} T^2 \left.\frac{\partial^2 G(\tau;\mu_q)}{\partial \mu_q^2}\right|_{\mu_q=0} + \mathcal{O}\left(\frac{\mu_q^3}{T^3}\right), \tag{3}$$

where $\mu_q = \mu_u = \mu_d$ is the quark chemical potential for the two light flavors. The chemical potential for the strange quark, μ_s, is set to zero, which is well justified [30,34,38]. Note that the quark and baryonic chemical potentials are trivially related via $\mu_B = 3\mu_q$. T dependence is suppressed throughout.

One can show that odd derivatives with respect to μ_q vanish [48], while the second derivative at $\mu_q = 0$ is

$$\left.\frac{\partial^2 G(\tau;\mu_q)}{\partial \mu_q^2}\right|_{\mu_q=0} \equiv G''(\tau) = \left\langle g''(\tau) + g\frac{\Delta''}{\Delta}\right\rangle_B - \langle g\rangle_B \left\langle \frac{\Delta''}{\Delta}\right\rangle_B. \tag{4}$$

TABLE II. Number of time slices and temperatures related via $T = 1/(a_\tau N_\tau)$, as well as $T/T_{\rm pc}$ and the number of lattice configurations in the Generation 2 and 2L ensembles.

Generation 2							
N_τ	40	36	32	28	24	20	16
T [MeV]	141	156	176	201	235	281	352
$T/T_{\rm pc}$	0.77	0.86	0.97	1.10	1.29	1.54	1.93
$N_{\rm cfg}$	501	501	1000	1001	1001	1001	1001
Generation 2L							
N_τ	40	36	32	28	24	20	16
T [MeV]	152	169	190	217	253	304	380
$T/T_{\rm pc}$	0.91	1.01	1.13	1.29	1.51	1.82	2.27
$N_{\rm cfg}$	1102	1119	1090	1031	1016	1030	1102

Here $\Delta = \det D[U, \mu_q]$ is the determinant for the two light quarks, the determinant for the strange quark is included (with $\mu_s = 0$) but not written explicitly, D is the Dirac operator, U is the gauge link variable and the primes denote derivatives with respect to μ_q. The full expression can be found in the Appendix of Ref. [48]. The numerically expensive part is the computation of the disconnected contribution, which we evaluate using around 2000 random Gaussian noise sources [40,50]. The correlators used in this work are presented in the Appendix.

III. RESULTS

From now on we focus on the vector and axial-vector correlators, which we denote here as G_V and G_A, with $\Gamma_H = \gamma_i$ and $\gamma_5\gamma_i$ respectively, summed over i; see Eq. (2). We consider these to second order,

$$G_{V/A}(\tau;\mu_q) = G_{V/A}(\tau) + \frac{1}{2}\mu_q^2 G''_{V/A}(\tau). \tag{5}$$

To probe the restoration of chiral symmetry, we introduce the following ratio [51]:

$$R(\tau;\mu_q) = \frac{\tilde{G}_V(\tau;\mu_q) - \tilde{G}_A(\tau;\mu_q)}{\tilde{G}_V(\tau;\mu_q) + \tilde{G}_A(\tau;\mu_q)}, \tag{6}$$

with $\tilde{G}_{V/A}(\tau;\mu_q) = G_{V/A}(\tau;\mu_q)/G_{V/A}(N_\tau/2;\mu_q)$, i.e., both $\tilde{G}_{V/A}(\tau;\mu_q)$ are normalized to unity at the midpoint of the temporal lattice, $\tau = N_\tau/2$. Note that the wave function renormalization $Z_{V/A}$ drops out of the ratios and that $R(\tau = N_\tau/2;\mu_q)$ is trivially zero.

In Fig. 1 we present the ratio $R(\tau;\mu_q)$ for the Generation 2 ensembles at seven different temperatures at $\mu_q = 0$ (above) and $\mu_q = 113$ MeV (below). We concentrate on the behavior near the centre of the lattice, $\tau T = 1/2$. Consider first low temperatures in the confined phase. Assuming a single-pole Ansatz for the vector and axial-vector correlators, with dimensionless masses $\tilde{m}_{V/A} = m_{V/A}/T$, Eq. (6) reads

$$\begin{aligned} R(\tau;0) &= \frac{\cosh(\tilde{m}_V x) - \cosh(\tilde{m}_A x)}{\cosh(\tilde{m}_V x) + \cosh(\tilde{m}_A x)} \\ &\approx \frac{1}{4T^2}(m_V^2 - m_A^2)x^2 + \mathcal{O}(x^4), \end{aligned} \tag{7}$$

where $x = \tau T - 1/2$ and the expansion is valid around the center of the lattice. Indeed, given that the (ground state) vector meson is lighter than the axial-vector meson, we observe in Fig. 1 an inverted parabola near the center of the lattice at the lower temperatures. Away from the center of the lattice, $R(\tau;\mu_q)$ is dominated by excited states and the short-distance behavior of Wilson fermions, which breaks chiral symmetry explicitly and will be discussed below.

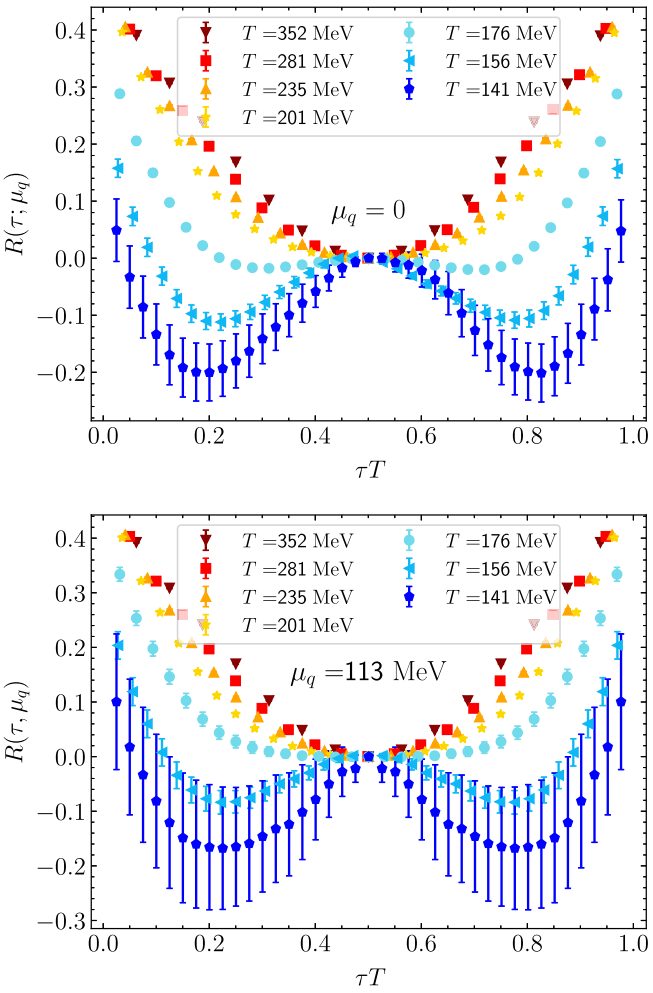

FIG. 1. Generation 2 results for $R(\tau;\mu_q)$ as defined in Eq. (6) for several temperatures at $\mu_q = 0$ (above) and $\mu_q = 113$ MeV (below).

Considering medium effects in the hadronic phase, the negative curvature is expected to depend on both the temperature and the chemical potential and to vanish when chiral symmetry is restored. Indeed, we observe a change in curvature as the temperature increases. Since we use Wilson fermions, we do not expect to see a complete degeneracy—$G_V(\tau) = G_A(\tau)$ and $R(\tau) = 0$ for all τ—even when chiral symmetry is restored. At high temperature, this can be analyzed by calculating $R(\tau;\mu_q)$ with noninteracting lattice quarks, using the same (Wilson) discretization and geometry as in the simulation [52]. Results for $R(\tau;0)$ obtained for free quarks and for the Generation 2 ensembles in the high-temperature phase are compared in Fig. 2. The noninteracting results are shown by the dashed lines (even though they are computed at the same discrete set of lattice points). We observe excellent agreement at the highest temperatures, indicating that the quarks are weakly interacting. More importantly, this result shows that the nondegeneracy is explained by the Wilson fermion discretization in the lattice action [52]. As a side note, for

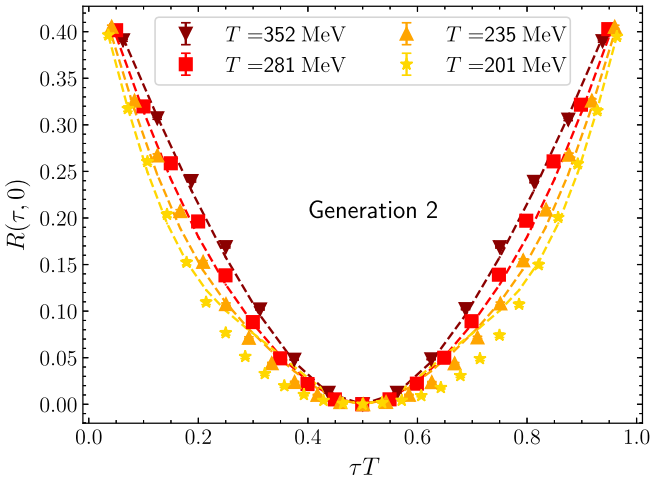

FIG. 2. Comparison between $R(\tau;0)$ on the Generation 2 ensembles in the high-temperature phase (symbols) and for noninteracting lattice fermions, using the same parameters and lattice geometry (dashed lines).

lattice actions with (a remnant of) chiral symmetry, such as staggered quarks, full degeneracy is observed at higher temperatures; see *e.g.* Fig. 1 of Ref. [53] for the case of $G_{PS}(\tau)$ and $G_S(\tau)$.

The above discussion gives us confidence that we understand the behavior of $R(\tau;\mu_q)$ both at low temperature, where $R(\tau;\mu_q)$ has a (local) maximum at $\tau T = 1/2$, and at high temperature, where it has a minimum. In between these two regimes, by necessity there is a temperature where the curvature of $R(\tau,\mu_q)$ at the center of the lattice vanishes. We use this point to define $T_{\rm pc}(\mu_q)$ in what follows. To quantitatively estimate the μ_q dependence of the pseudocritical temperature, we define the time-averaged quantity [44,54],

$$\bar{R}(\mu_q,T) = \frac{\sum_{\tau=\tau_{\rm min}}^{N_\tau/2} R(\tau;\mu_q,T)/\sigma^2(\tau;\mu_q,T)}{\sum_{\tau=\tau_{\rm min}}^{N_\tau/2} 1/\sigma^2(\tau;\mu_q,T)}, \qquad (8)$$

where $\sigma^2(\tau)$ is the variance at time τ, and we have reintroduced the previously implicit dependence of R on T. $R(\tau)$ is symmetric about $N_\tau/2$, and hence we use $N_\tau/2$ as the upper limit in the sum. The value of $\tau_{\rm min}$ is chosen so that $\tau_{\rm min}T \approx 0.2$ for all temperatures and for both Generation 2 and Generation 2L data. This value is selected to suppress unwanted effects due to the short-distance behavior of Wilson fermions and excited states; see Fig. 1. At fixed μ_q, we then interpolate $\bar{R}(\mu_q,T)$ with T using a cubic spline and find $T_{\rm pc}(\mu_q)$ from the x-intercept, i.e., $\bar{R}(\mu_q,T_{\rm pc}) = 0$. We note that this method uses the correlation functions directly and does not require a fit.

Examples of this procedure are shown in Fig. 3 for both Generation 2 and 2L ensembles and at $\mu_q = 0$ and 56 MeV. We also show the value of $T_{\rm pc}(0)$ found independently

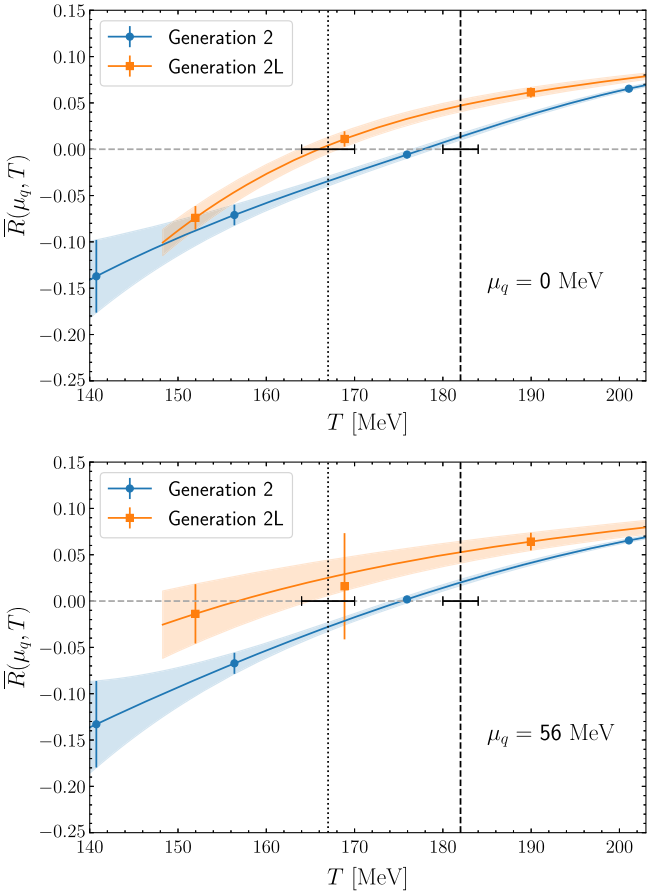

FIG. 3. Averaged ratio $\bar{R}(\mu_q,T)$ as defined in Eq. (8), plotted against the temperature, for $\mu_q = 0$ (above) and $\mu_q = 56$ MeV (below). Blue (orange) symbols correspond to Generation 2 (2L) and the blue (orange) curves show the corresponding interpolating curves obtained using cubic splines. The dashed (dotted) vertical lines correspond to $T_{\rm pc}(\mu_q = 0)$ obtained from the renormalized chiral condensate for Generation 2 (2L), including the error estimate; see Table I. The μ_q-dependent pseudocritical temperature is determined by $\bar{R}(\mu_q,T_{\rm pc}) = 0$ and decreases with μ_q.

using the renormalized chiral condensate $\langle\bar{\psi}\psi\rangle_R$ [55]. As μ_q increases, the intercept moves to smaller values of T, reducing the pseudocritical temperature. It is evident from the lower plot in Fig. 3 that the error bars on the Generation 2L data points are larger than for Generation 2, especially near $T_{\rm pc}$. This is mainly due to the smaller pion mass in the gauge ensembles. Moreover, the Generation 2L ensemble at $T = 169$ MeV sits, within errors, at the value of $T_{\rm pc}$ obtained via the renormalized chiral condensate. This leads to large fluctuations and adds no meaningful information. We hence have excluded this point from the analysis.

The values for $T_{\rm pc}(\mu_q)$ obtained from this method for several values of μ_q are shown in Fig. 4 and Table III for both Generation 2 and 2L. The gray and black dots in Fig. 4 correspond to the value of $T_{\rm pc}(0)$ obtained via the renormalized chiral condensate; see Table I. Also shown is the

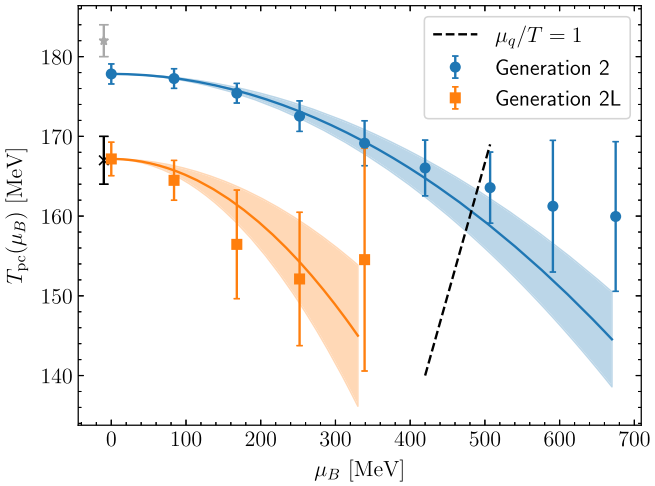

FIG. 4. Pseudocritical temperature as a function of μ_B from the Generation 2 (2L) ensembles shown by blue circles (orange squares). The blue (orange) curve is the fit of the data points to Eq. (1) for Generation 2 (2L). The $T_{pc}(0)$ values obtained from the renormalized chiral condensate are shown as gray (black) crosses for generation 2 (2L); see Table I. The dashed line is $\mu_q/T = 1$ which sets a limit on the applicability of the Taylor expansion, Eq. (3).

line $\mu_q/T = 1$, which sets a limit on the applicability of the Taylor expansion, Eq. (3).

We fit the $T_{\rm pc}(\mu_q)$ values to Eq. (1) to determine κ, obtaining the values shown in the bottom line of Table III. Our results for κ together with those from other groups are plotted in Fig. 5. For the Generation 2 ensembles, we note good agreement between our hadronic method and those using the renormalized chiral condensate. This agreement may be somewhat of a happy accident, as we have used one lattice spacing with unphysical light quarks, whereas the other results have been obtained in the continuum limit, with (partially) chirally symmetric actions, at or close to the physical point. Concerning Generation 2L, the lighter pion mass makes the calculation more challenging computationally which is reflected in a higher associated uncertainty. As stated, one of the ensembles sits very close to the transition, influencing the result strongly when included, while excluding it reduces the available data and hence increases the uncertainty.

TABLE III. Pseudocritical temperature $T_{\rm pc}(\mu_q)$ determined using Eq. (8) for different values of $\mu_B = 3\mu_q$, for both the Generation 2 and 2L ensembles, including the values of κ obtained from the fit to Eq. (1). The results for $T_{\rm pc}(0)$ obtained from the renormalized chiral condensate are $T_{\rm pc}(0) = 182(2)$ and $T_{\rm pc}(0) = 167(3)$ for Generation 2 and 2L respectively, see Table I. The first error is statistical while the second is systematic. The value of κ obtained using Generation 2L ensembles is dominated entirely by the statistical error.

		Generation 2	Generation 2L
μ_q [MeV]	μ_B [MeV]	$T_{\rm pc}(\mu_q)$ [MeV]	$T_{\rm pc}(\mu_q)$ [MeV]
0	0	177.8(1.2)(5.8)	167.1(2.1)(3.1)
28	84	177.2(1.2)(5.7)	164.5(2.5)(3.1)
56	168	175.4(1.2)(5.5)	156.5(6.8)(0.8)
84	252	172.5(1.9)(3.9)	152.1(8.4)(0.9)
113	339	169.1(2.8)(1.5)	155(14)(2.0)
140	420	166.2(3.5)(0.6)	
	κ	0.0131(23)(23)	0.034(14)

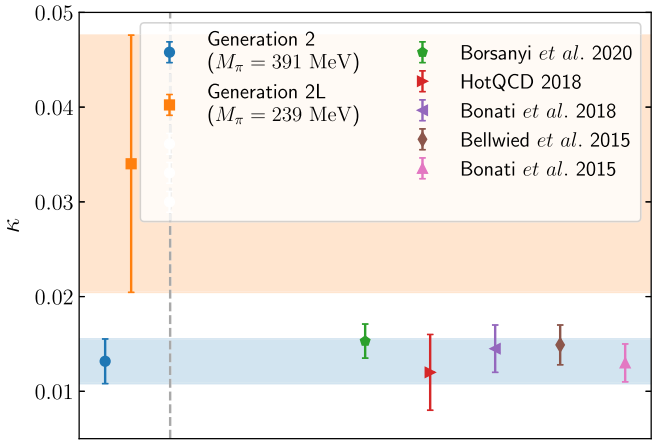

FIG. 5. Final results for κ obtained using Generation 2 (blue circle, $M_\pi = 391(3)$ MeV) and Generation 2L (orange square, $M_\pi = 239(1)$ MeV) compared with results from Refs. [4,5,34,36,39].

Additionally, we note that, in principle, the curvatures in the $T - \mu_B$ plane could be different for different quantities since the transition is a crossover. If a critical end point exists, the transition lines would eventually coincide, however, the values of μ_B explored in this study are still too far away from any such putative critical end point to make a judgement on this.

IV. SYSTEMATICS

A. Finite volume effects

In this section we discuss the systematics which could affect the result of our analysis. We start with finite-volume effects. To investigate the finite volume dependence, we produced correlation functions using a larger spatial volume for our Generation 2 ensemble at $T = 201$ MeV ($N_\tau = 28$), with the number of spatial lattice sites increased from $N_s = 24$ to $N_s = 32$. In Fig. 6 we show results for $R(\tau;\mu_q)$, defined in Eq. (6), for the two different volumes and for two different values of μ_q. The negligible effect of increasing the volume is confirmed also on the averaged quantity $\bar{R}$, shown in Fig. 7. The effect of changing the spatial volume gives results that are compatible well within the quoted statistical error for all μ_q values considered, and hence we do not include it in the final error budget.

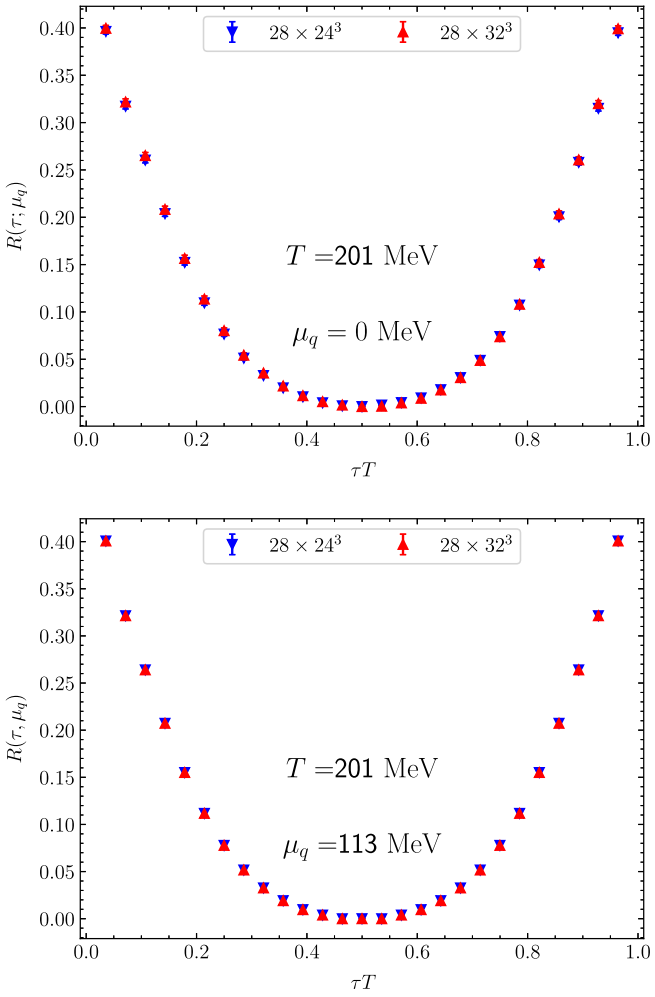

FIG. 6. $R(\tau;\mu_q)$ ratio as defined in Eq. (6) obtained using different volumes of the Generation 2 ensembles, for $\mu_q = 0$ (above) and $\mu_q = 113$ MeV (below) at fixed $T = 201$ MeV.

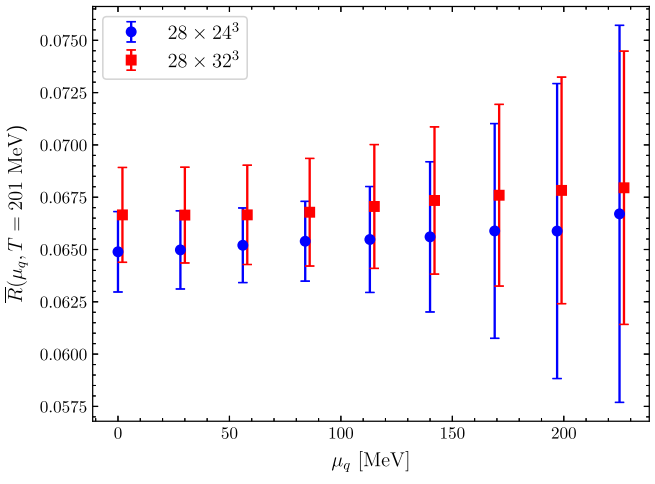

FIG. 7. $\bar{R}(\mu_q, T)$ ratio as defined in Eq. (8) at $T = 201$ MeV as a function of μ_q. The blue circles and red squares correspond respectively to the spatial volume $N_s^3 = 24^3$ and $N_s^3 = 32^3$.

B. Changing τ_{min}

We now turn our attention to the choice of τ_{min}. The default choices for τ_{min}/a_τ are $[3,4,4,5,6,7,7]$ and $[2,3,3,4,5,6,7]$ for Generation 2 and Generation 2L respectively, where the values are ordered from the smallest N_τ to the largest, *i.e.* $N_\tau = [16,20,24,28,32,36,40]$. These values upon multiplication with the temperature give a value which corresponds roughly to $\tau_{\text{min}} T \approx 0.2$. Below we explore different cases in which we increase the value of τ_{min} up to $\tau_{\text{min}}^{\text{default}} + 3$ (we put $a_\tau = 1$ temporarily for notational convenience). Figure 8 shows the value of $\bar{R}(\mu_q, T)$ for different choices of τ_{min}. Below and up to T_{pc} the results are mostly compatible within the statistical errors. This is the main region of interest since we determine the degeneracy of the vector and axial-vector channel at the point in which $\bar{R}$ crosses zero. As the temperature increases, the ratio becomes successively more

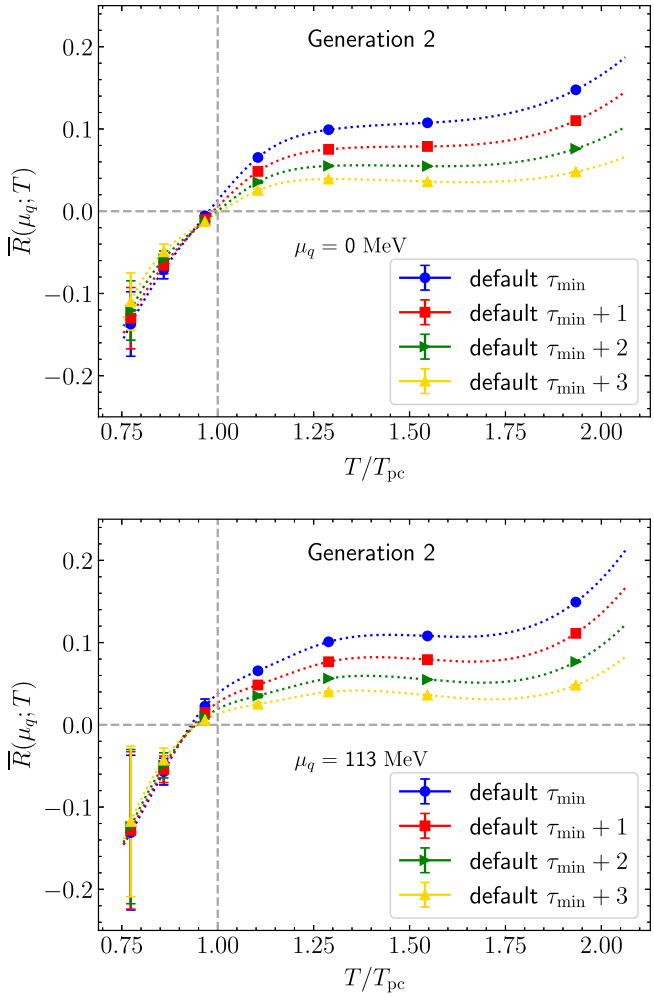

FIG. 8. Generation 2 results for $\bar{R}(\mu_q, T)$ as a function of the temperature and for different choices of τ_{min}. The top and bottom plots show respectively the results at $\mu_q = 0$ and $\mu_q = 113$ MeV. The vertical gray line shows the value of T_{pc} determined using the renormalized chiral condensate.

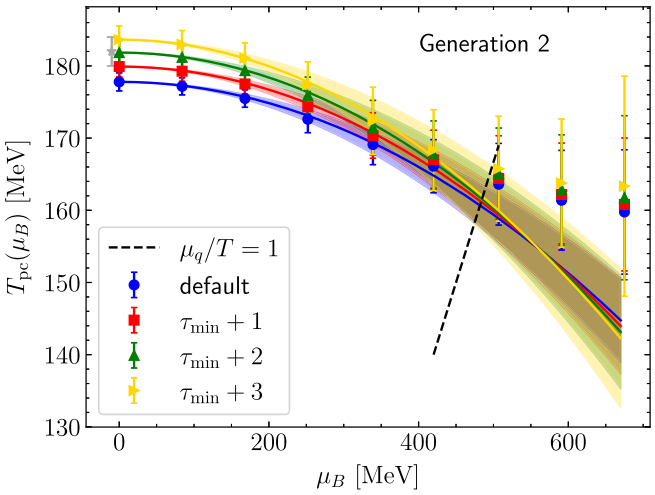

FIG. 9. The pseudocritical temperature as a function of μ_B for different choices of $\tau_{\rm min}$, from the Generation 2 ensembles. Similar results are obtained with Generation 2L ensembles.

sensitive to short-distance lattice artifacts of Wilson quarks, due to the choice of $\tau_{\rm min}$.

To compute the systematic error coming from varying $\tau_{\rm min}$ we use the following formula [56]:

$$\Delta_{\rm sys} = \max\left[\Delta_{\rm tot}\mathcal{P}_{\rm sys}\mathrm{erf}\left(\frac{\mathcal{P}_{\rm sys}}{\sqrt{2}}\right)\right], \tag{9}$$

with $\Delta_{\rm tot} = \sqrt{(\Delta T_{\rm pc}^{\rm default})^2 + (\Delta T_{\rm pc}^{\tau_{\rm min}})^2}$ and $\mathcal{P}_{\rm sys} = |T_{\rm pc}^{\rm default} - T_{\rm pc}^{\tau_{\rm min}}|/\Delta_{\rm tot}$. In the expression above, $\Delta T_{\rm pc}^{\rm default}$ and $\Delta T_{\rm pc}^{\tau_{\rm min}}$ are respectively the statistical error of the pseudocritical temperature obtained using the default settings and using the value of $\tau_{\rm min}$ which shows the largest discrepancy from the default value. The pull variable $\mathcal{P}_{\rm sys}$ indicates how significant the systematic error is over the statistical error.

We investigated the systematic effect of varying $\tau_{\rm min}$ also on our fits of the pseudocritical line to extract the value of κ. In Fig. 9 we show the fits for the Generation 2 ensembles and in Table IV we report the corresponding results for κ. Similar results are obtained with Generation 2L ensembles, where the final result for κ is entirely dominated by statistical errors.

TABLE IV. Values of κ extracted by fitting the results of $T_{\rm pc}$ obtained for different values of $\tau_{\rm min}$ with Generation 2 ensembles.

$\tau_{\rm min}$	κ
default $\tau_{\rm min}$	0.0131(23)
default $\tau_{\rm min} + 1$	0.0144(27)
default $\tau_{\rm min} + 2$	0.0156(32)
default $\tau_{\rm min} + 3$	0.0169(39)

Even though the determination of $T_{\rm pc}$ is affected by the choice of $\tau_{\rm min}$, the value of κ that we extract from our fits is rather stable, indicating that the $\tau_{\rm min}$ dependence is under control. The systematic error on the values of $T_{\rm pc}$ obtained through our analysis is reported in Table III, and the systematic error for κ is included in Fig. 5.

V. CONCLUSION

In this work we presented a novel approach to study the curvature of the pseudocritical temperature, $T_{\rm pc}(\mu_B)$, with baryon chemical potential using meson correlation function obtained from lattice QCD. We defined $T_{\rm pc}(\mu_B)$ via the degeneracy in the vector and axial-vector channels. The method employs the correlation functions directly and does not require fits.

We compared our results to those obtained elsewhere in the literature, finding good agreement especially for the results obtained from the Generation 2 ensembles, see Fig. 5, even though our ensembles have pions heavier than in nature, and our results are not extrapolated to the continuum. Nevertheless, it is intriguing that our method, based on hadronic correlation functions, gives similar results to the ones obtained with completely different observables, such as the renormalized chiral condensate and the strange quark number susceptibility.

In Sec. IV we assessed the systematic effects due to finite volume and our choice of $\tau_{\rm min}$. We find no sizeable finite-size effects, while an estimate for the systematic uncertainty coming from varying $\tau_{\rm min}$ is provided.

The lighter pion mass of the Generation 2L ensemble causes the correlation functions, especially the disconnected contributions, to be much noisier than for Generation 2, in particular near the pseudocritical point. The main contribution to the overall uncertainty of our results comes from the noisy disconnected contributions. It will be interesting to study the effect of using a different type of noise, *e.g.* Z_2 and Z_4 combined with different methods for noise reduction [57,58].

In the near future we plan to determine spectral functions to investigate the effects of chemical potential on the mesonic channels in order to obtain independent verification of our results.

ACKNOWLEDGMENTS

We are grateful to the HadSpec Collaboration for the use of their zero temperature ensembles. This work is supported by the UKRI Science and Technology Facilities Council (STFC) Consolidated Grant No. ST/X000648/1. We are grateful to Supercomputing Wales for the use of their computing resources and to the Swansea Academy for Advanced Computing for support. R. B. acknowledges support from a Science Foundation Ireland Frontiers for the Future Project award with Grant No. SFI-21/FFP-P/10186. This work used the DiRAC Data Intensive service

(DIaL2 / DIaL2.5) at the University of Leicester, managed by the University of Leicester Research Computing Service on behalf of the STFC DiRAC HPC Facility ([59]). The DiRAC service at Leicester was funded by BEIS, UKRI and STFC capital funding and STFC operations grants. It also used the DiRAC Blue Gene Q Shared Petaflop system at the University of Edinburgh, operated by the Edinburgh Parallel Computing Centre on behalf of the STFC DiRAC HPC Facility ([59]). This equipment was funded by BIS National E-infrastructure Capital Grant No. ST/K000411/1, STFC Capital Grant No. ST/H008845/1, and STFC DiRAC Operations Grants No. ST/K005804/1 and No. ST/K005790/1. DiRAC is part of the National E-Infrastructure. This work used the computing resources of the Irish Centre for High-End Computing (ICHEC). This work was performed using the PRACE Marconi-KNL resources hosted by CINECA, Italy. We acknowledge EuroHPC Joint Undertaking for awarding the project EHPC-EXT-2023E01-010 access to LUMI-C, Finland. S. K. is supported by the National Research Foundation of Korea under Grant No. NRF-2021R1A2C1092701 funded by the Korean government (MEST) and by the Institute of Information & Communication Technology Planning & Evaluation grant funded by the Korean government (Ministry of Science and ICT) (Grant No. IITP-2024-RS-2024-00437191).

A. S.: data analysis, physics interpretation, plot generation and primary manuscript production. C. A.: analysis idea, physics interpretations of results, and draft of the manuscript. G. A.: contributions to analysis, physics interpretations of results, and manuscript. R. B., B. J., J.-I. S.: data production and contribution to the manuscript. S. N., S. K., L. K. W.: conceptual ideas and contribution to the manuscript.

DATA AVAILABILITY

The data that support the findings of this article are openly available [60]. Gen 2 data can be found in Ref. [42]. Gen 2L ensembles are available on request. Details of the code and data presented can be found in Refs. [60,61].

APPENDIX: LATTICE CORRELATORS

In this appendix we show the correlators used to produce the main results in this paper and compare them with free correlators. In particular, we expand the discussion in Ref. [40], where similar plots for the correlators are shown. The plots showing correlator ratios are new.

Figure 10 shows the vector and axial-vector correlators for selected temperatures and for two different values of μ_q, in lattice units. As expected, for temperatures below $T_{\rm pc}$ the axial-vector correlator decreases exponentially faster than the vector one, indicating a heavier ground state. This behavior is lost near $T_{\rm pc}$, where the two correlators look very similar. For temperatures above $T_{\rm pc}$ the correlators are closer near the midpoint. The effect of a nonzero chemical potential is hard to gauge from these plots, with the only visible effect shown by the axial-vector correlator below $T_{\rm pc}$ exhibiting a worse signal-to-noise ratio near the midpoint.

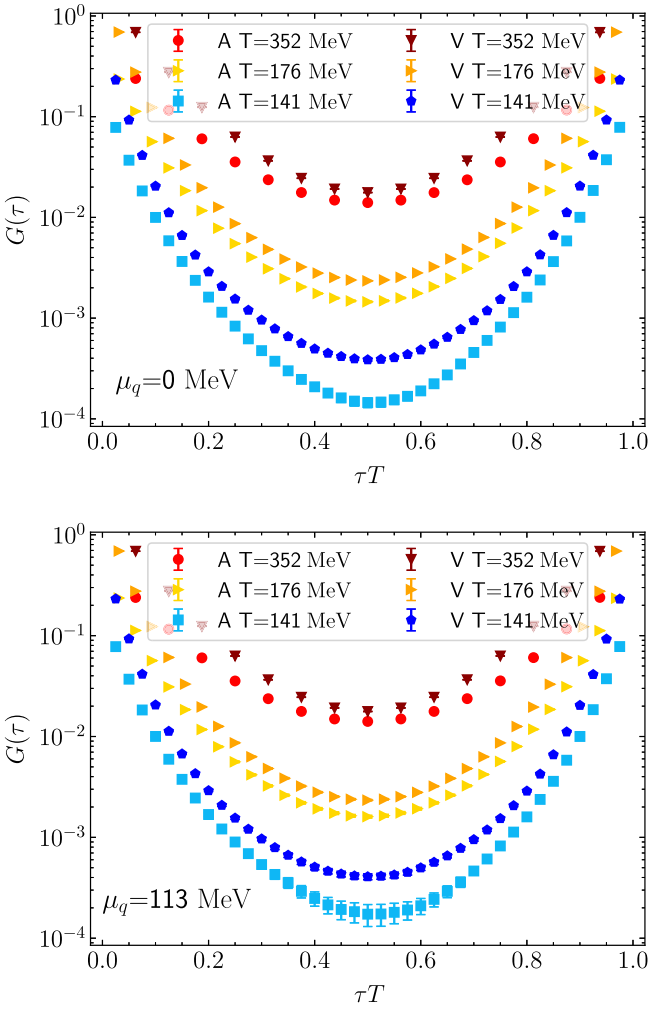

FIG. 10. Generation 2 vector and axial-vector correlators, in lattice units, for $\mu_q = 0$ (above) and $\mu_q = 113$ MeV (below) at temperatures below ($T = 141$ MeV), near ($T = 176$ MeV) and above ($T = 352$ MeV) the pseudocritical temperature obtained with the renormalized chiral condensate, $T_{\rm pc} = 182(2)$ MeV.

The correlators used in this study are obtained using local currents with Wilson fermions and need to be renormalized. To remove the dependence on the renormalization when comparing the vector and axial-vector correlators, we normalize the correlators with respect to the temporal midpoint. Figure 11 shows the normalized vector and axial-vector correlators $G_{V/A}(\tau;\mu_q)/G_{V/A}(N_\tau/2;\mu_q)$ for selected temperatures and for two different values of μ_q. Below $T_{\rm pc}$, the axial-vector correlator shows a stronger curvature compared to the vector

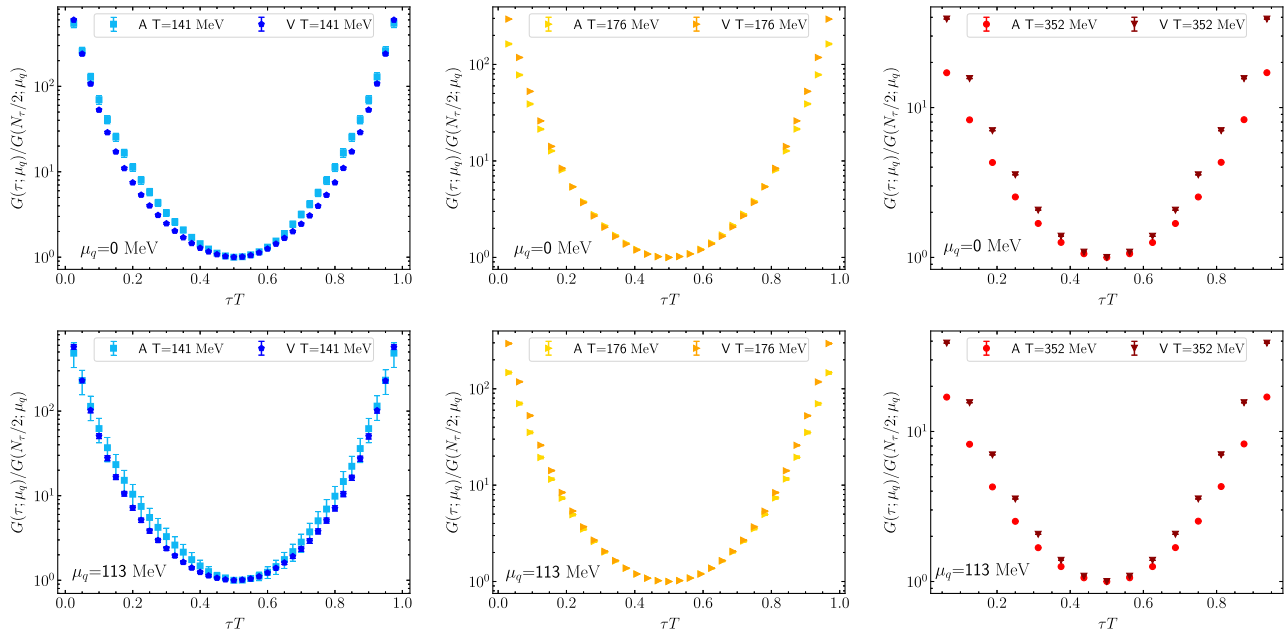

FIG. 11. As in the preceding figure, with normalized correlators $G_{V/A}(\tau;\mu_q)/G_{V/A}(N_\tau/2;\mu_q)$.

correlator around the midpoint, consistent with a larger ground state mass. Near $T_{\rm pc}$, the correlators are nearly degenerate, except near the edges where short-distance effects and lattice artifacts dominate. At high temperature, lattice artifacts are even more pronounced due to the short temporal extent. Lattice artifacts affect the axial-vector and vector correlators differently as can be understood from the corresponding free correlators [52]. Increasing μ_q pushes the axial-vector correlator closer to the vector one while also introducing more noise. The effect of a nonzero μ_q is barely noticeable in Figs. 10 and 11. In the main paper we use the ratio defined in Eq. (6) to bring out the T and μ_q dependence more prominently; see Fig. 1.

Finally, in Fig. 12 we compare the correlators with the free correlators obtained using the same lattice geometry [52], in lattice units (left) and using the ratio $G_{V/A}(\tau)/G^{\rm free}_{V/A}(\tau)$ (right). Since the wave function normalization is not included, there is an undetermined multiplicative factor. In the axial-vector channel, at this temperature good agreement between the full and the free correlator can be seen, with deviations up to around 10%. In the vector channel, we observe a deviation between the full and the free correlator, which can be incorporated by adding a constant term to the free correlator. We determine this constant simply as the difference at the midpoint, $G_V^{\rm LQCD}(N_\tau/2) - G_V^{\rm free}(N_\tau/2)$, which improves the comparison. The origin of

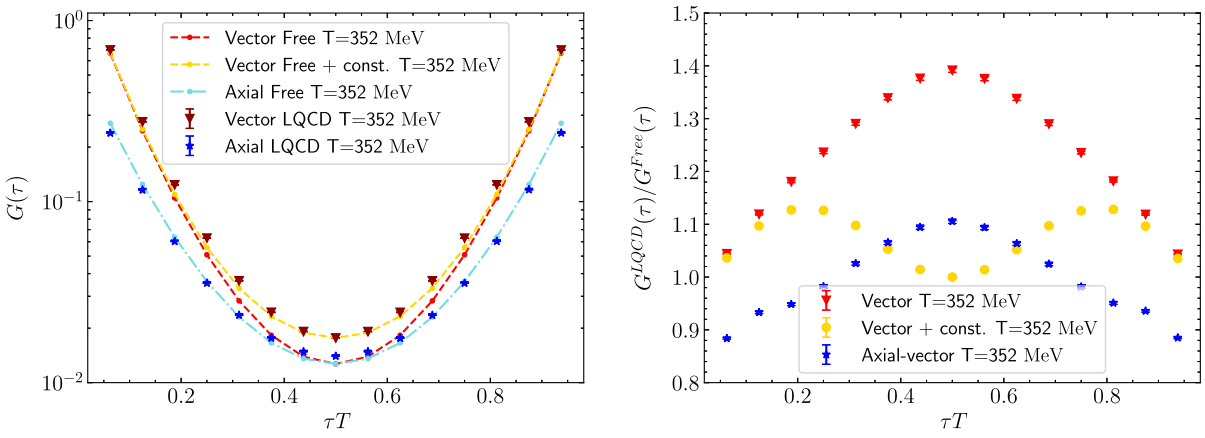

FIG. 12. Generation 2 vector and axial-vector correlators obtained in the full lattice QCD simulation and in the free theory, at $\mu_q = 0$. Shown are correlators in lattice units (left) and ratio $G_{V/A}(\tau)/G^{\rm free}_{V/A}(\tau)$ (right). In the vector channel, both the free correlator and the free correlator plus a constant, with const $= G_V^{\rm LQCD}(N_\tau/2) - G_V^{\rm free}(N_\tau/2)$, are shown.

this shift may be due to the transport contribution. In the noninteracting case, the transport contribution to the spectral function in the vector channel reads [62] $\rho_{\text{transport}}(\omega) = 2\pi N_c I \omega \delta(\omega)$, where in the massless limit, $I = T^2/3$. This contribution yields a τ-independent constant factor to the correlator, $G_{\text{transport}}(\tau) = N_c I T$. The additional shift can then be attributed to a more pronounced transport peak, indicating that at this temperature, interaction effects remain present. It is worth noting that the electrical conductivity was studied in detail on the Generation 2 ensembles in Ref. [41] and hence we do not study it further here.

[1] F. Karsch, Critical behavior and net-charge fluctuations from lattice QCD, Proc. Sci. CORFU2018 (**2019**) 163 [arXiv:1905.03936].

[2] Wuppertal-Budapest Collaboration, Is there still any T_c mystery in lattice QCD? Results with physical masses in the continuum limit III, J. High Energy Phys. 09 (2010) 073.

[3] A. Bazavov *et al.*, The chiral and deconfinement aspects of the QCD transition, Phys. Rev. D **85**, 054503 (2012).

[4] HotQCD Collaboration, Chiral crossover in QCD at zero and non-zero chemical potentials, Phys. Lett. B **795**, 15 (2019).

[5] S. Borsanyi, Z. Fodor, J. N. Guenther, R. Kara, S. D. Katz, P. Parotto, A. Pasztor, C. Ratti, and K. K. Szabó, QCD crossover at finite chemical potential from lattice simulations, Phys. Rev. Lett. **125**, 052001 (2020).

[6] C. R. Allton, S. Ejiri, S. J. Hands, O. Kaczmarek, F. Karsch, E. Laermann, Ch. Schmidt, and L. Scorzato, The QCD thermal phase transition in the presence of a small chemical potential, Phys. Rev. D **66**, 074507 (2002).

[7] R. V. Gavai and S. Gupta, QCD at finite chemical potential with six time slices, Phys. Rev. D **78**, 114503 (2008).

[8] M. Stephanov, K. Rajagopal, and E. Shuryak, Signatures of the tricritical point in QCD, Phys. Rev. Lett. **81**, 4816 (1998).

[9] P. de Forcrand, Simulating QCD at finite density, Proc. Sci. LAT2009 (**2009**) 010 [arXiv:1005.0539].

[10] G. Aarts, Introductory lectures on lattice QCD at nonzero baryon number, J. Phys. Conf. Ser. **706**, 022004 (2016).

[11] M. G. Alford, A. Kapustin, and F. Wilczek, Imaginary chemical potential and finite fermion density on the lattice, Phys. Rev. D **59**, 054502 (1999).

[12] M.-P. Lombardo, Finite density (might well be easier) at finite temperature, Nucl. Phys. B, Proc. Suppl. **83**, 375 (2000).

[13] P. de Forcrand and O. Philipsen, The QCD phase diagram for small densities from imaginary chemical potential, Nucl. Phys. **B642**, 290 (2002).

[14] P. de Forcrand and O. Philipsen, The chiral critical point of $N(f) = 3$ QCD at finite density to the order $(\mu/T)^4$, J. High Energy Phys. 11 (2008) 012.

[15] M. D'Elia and M.-P. Lombardo, Finite density QCD via imaginary chemical potential, Phys. Rev. D **67**, 014505 (2003).

[16] M. D'Elia and M. P. Lombardo, QCD thermodynamics from an imaginary $\mu(B)$: Results on the four flavor lattice model, Phys. Rev. D **70**, 074509 (2004).

[17] V. Azcoiti, G. Di Carlo, A. Galante, and V. Laliena, Phase diagram of QCD with four quark flavors at finite temperature and baryon density, Nucl. Phys. **B723**, 77 (2005).

[18] H.-S. Chen and X.-Q. Luo, Phase diagram of QCD at finite temperature and chemical potential from lattice simulations with dynamical Wilson quarks, Phys. Rev. D **72**, 034504 (2005).

[19] P. Cea, L. Cosmai, M. D'Elia, and A. Papa, The critical line from imaginary to real baryonic chemical potentials in two-color QCD, Phys. Rev. D **77**, 051501 (2008).

[20] L.-K. Wu, X.-Q. Luo, and H.-S. Chen, Phase structure of lattice QCD with two flavors of Wilson quarks at finite temperature and chemical potential, Phys. Rev. D **76**, 034505 (2007).

[21] K. Nagata and A. Nakamura, Imaginary chemical potential approach for the pseudo-critical line in the QCD phase diagram with clover-improved Wilson fermions, Phys. Rev. D **83**, 114507 (2011).

[22] P. Cea, L. Cosmai, M. D'Elia, C. Manneschi, and A. Papa, Analytic continuation of the critical line: Suggestions for QCD, Phys. Rev. D **80**, 034501 (2009).

[23] A. Alexandru and A. Li, QCD at imaginary chemical potential with Wilson fermions, Proc. Sci. LATTICE2013 (**2014**) 208 [arXiv:1312.1201].

[24] P. Cea, L. Cosmai, M. D'Elia, A. Papa, and F. Sanfilippo, The critical line of two-flavor QCD at finite isospin or baryon densities from imaginary chemical potentials, Phys. Rev. D **85**, 094512 (2012).

[25] P. Alba *et al.*, Constraining the hadronic spectrum through QCD thermodynamics on the lattice, Phys. Rev. D **96**, 034517 (2017).

[26] V. Vovchenko, A. Pásztor, Z. Fodor, S. D. Katz, and H. Stoecker, Repulsive baryonic interactions and lattice QCD observables at imaginary chemical potential, Phys. Lett. B **775**, 71 (2017).

[27] R. V. Gavai and S. Gupta, Pressure and nonlinear susceptibilities in QCD at finite chemical potentials, Phys. Rev. D **68**, 034506 (2003).

[28] B.-J. Schaefer and J. Wambach, The phase diagram of the quark meson model, Nucl. Phys. **A757**, 479 (2005).

[29] C. R. Allton, M. Döring, S. Ejiri, S. J. Hands, O. Kaczmarek, F. Karsch *et al.*, Thermodynamics of two flavor QCD to sixth order in quark chemical potential, Phys. Rev. D **71**, 054508 (2005).

[30] M. D'Elia, High-Temperature QCD: Theory overview, Nucl. Phys. **A982**, 99 (2019).

[31] O. Kaczmarek, F. Karsch, E. Laermann, C. Miao, S. Mukherjee, P. Petreczky *et al.*, Phase boundary for the chiral transition in $(2+1)$ -flavor QCD at small values of the chemical potential, Phys. Rev. D **83**, 014504 (2011).
[32] G. Endrődi, Z. Fodor, S. D. Katz, and K. K. Szabo, The QCD phase diagram at nonzero quark density, J. High Energy Phys. 04 (2011) 001.
[33] P. Cea, L. Cosmai, and A. Papa, Critical line of $2+1$ flavor QCD, Phys. Rev. D **89**, 074512 (2014).
[34] C. Bonati, M. D'Elia, M. Mariti, M. Mesiti, F. Negro, and F. Sanfilippo, Curvature of the chiral pseudocritical line in QCD, Phys. Rev. D **90**, 114025 (2014).
[35] C. Bonati, M. D'Elia, M. Mariti, M. Mesiti, F. Negro, and F. Sanfilippo, Curvature of the chiral pseudocritical line in QCD: Continuum extrapolated results, Phys. Rev. D **92**, 054503 (2015).
[36] R. Bellwied, S. Borsanyi, Z. Fodor, J. Günther, S. D. Katz, C. Ratti, and K. K. Szabo, The QCD phase diagram from analytic continuation, Phys. Lett. B **751**, 559 (2015).
[37] P. Cea, L. Cosmai, and A. Papa, Critical line of $2+1$ flavor QCD: Toward the continuum limit, Phys. Rev. D **93**, 014507 (2016).
[38] HotQCD Collaboration, The QCD crossover at zero and non-zero baryon densities from lattice QCD, Nucl. Phys. **A982**, 847 (2019).
[39] C. Bonati, M. D'Elia, F. Negro, F. Sanfilippo, and K. Zambello, Curvature of the pseudocritical line in QCD: Taylor expansion matches analytic continuation, Phys. Rev. D **98**, 054510 (2018).
[40] A. Nikolaev, G. Aarts, C. Allton, D. De Boni, J. Glesaaen, S. Hands *et al.*, Mesonic correlators at non-zero baryon chemical potential, Proc. Sci. LATTICE2019 (**2020**) 077 [arXiv:2001.04415].
[41] G. Aarts, C. Allton, A. Amato, P. Giudice, S. Hands, and J.-I. Skullerud, Electrical conductivity and charge diffusion in thermal QCD from the lattice, J. High Energy Phys. 02 (2015) 186.
[42] G. Aarts, C. Allton, A. Amato, R. Bignell, T. J. Burns, D. De Boni *et al.*, Fastsum generation 2 anisotropic thermal lattice QCD gauge ensembles (2023), 10.5281/zenodo.8403827.
[43] G. Aarts, C. Allton, R. Bignell, T. J. Burns, S. C. García-Mascaraque, S. Hands *et al.*, Open charm mesons at nonzero temperature: Results in the hadronic phase from lattice QCD, arXiv:2209.14681.
[44] G. Aarts, C. Allton, M. N. Anwar, R. Bignell, T. J. Burns, B. Jäger, and J.-I. Skullerud, Non-zero temperature study of spin $1/2$ charmed baryons using lattice gauge theory, Eur. Phys. J. A **60**, 59 (2024).
[45] FASTSUM Collaboration, Fastsum Generation 2L Anisotropic Thermal Lattice QCD Gauge Ensembles (2024), https://10.5281/zenodo.10636046.
[46] Hadron Spectrum Collaboration, Flavor structure of the excited baryon spectra from lattice QCD, Phys. Rev. D **87**, 054506 (2013).
[47] D. J. Wilson, R. A. Briceno, J. J. Dudek, R. G. Edwards, and C. E. Thomas, The quark-mass dependence of elastic πK scattering from QCD, Phys. Rev. Lett. **123**, 042002 (2019).
[48] QCD-TARO Collaboration, Responses of hadrons to chemical potential at finite temperature, Phys. Rev. D **65**, 054501 (2002).
[49] QCD-TARO Collaboration, Properties of hadron screening masses at finite baryonic density, Phys. Lett. B **609**, 265 (2005).
[50] SESAM Collaboration, Evaluating sea quark contributions to flavor singlet operators in lattice QCD, Phys. Lett. B **389**, 720 (1996).
[51] S. Datta, S. Gupta, M. Padmanath, J. Maiti, and N. Mathur, Nucleons near the QCD deconfinement transition, J. High Energy Phys. 02 (2013) 145.
[52] G. Aarts and J. M. Martínez Resco, Continuum and lattice meson spectral functions at nonzero momentum and high temperature, Nucl. Phys. **B726**, 93 (2005).
[53] G. Aarts, C. Allton, J. Foley, S. Hands, and S. Kim, Meson spectral functions at nonzero momentum in hot QCD, Nucl. Phys. **A785**, 202 (2007).
[54] G. Aarts, C. Allton, S. Hands, B. Jäger, C. Praki, and J.-I. Skullerud, Nucleons and parity doubling across the deconfinement transition, Phys. Rev. D **92**, 014503 (2015).
[55] G. Aarts *et al.*, Properties of the QCD thermal transition with $\mathrm{Nf} = 2+1$ flavors of Wilson quark, Phys. Rev. D **105**, 034504 (2022).
[56] (Extended Twisted Mass Collaboration ETMC), Probing the energy-smeared R ratio using lattice QCD, Phys. Rev. Lett. **130**, 241901 (2023).
[57] G. S. Bali, S. Collins, and A. Schäfer, Effective noise reduction techniques for disconnected loops in lattice QCD, Comput. Phys. Commun. **181**, 1570 (2010).
[58] L. Giusti, T. Harris, A. Nada, and S. Schaefer, Frequency-splitting estimators of single-propagator traces, Eur. Phys. J. C **79**, 586 (2019).
[59] https://www.dirac.ac.uk
[60] A. Smecca, G. Aarts, C. Allton, R. Bignell, B. Jäger, S.-I. Nam *et al.*, The curvature of the pseudocritical line in the QCD phase diagram from mesonic lattice correlation functions—data release, (2024)10.5281/zenodo.14876523.
[61] A. Smecca, G. Aarts, C. Allton, R. Bignell, B. Jaeger, S.-I. Nam *et al.*, mu2_curvature, https://github.com/asmecca/mu2_curvature (2025).
[62] G. Aarts and A. Nikolaev, Electrical conductivity of the quark-gluon plasma: Perspective from lattice QCD, Eur. Phys. J. A **57**, 118 (2021).